13
Disorder Effects in the Raman Spectra of sp^2 Carbons

In general, disorder-induced symmetry-breaking plays a very important role in the determination of several materials properties such as transport properties and the relaxation of photoexcited carriers. In particular, sp^2 carbons which have high symmetry are sensitive to symmetry-breaking defects. Disorder and symmetry-breaking are observed sensitively by spectroscopy which depends strongly on crystal symmetry [95, 118]. The presence of disorder in sp^2 hybridized carbon systems, leads to rich and intriguing phenomena in their resonance Raman spectra, thus making Raman spectroscopy one of the most sensitive and informative techniques to characterize disorder in sp^2 carbon materials. Raman spectroscopy has thus become a key tool and is widely used to identify disorder in the sp^2-network of different carbon structures, such as diamond-like carbon, amorphous carbon, nanostructured carbon, as well as carbon nanofibers, nanotubes and nanohorns [20, 168, 394].

Figure 13.1a shows the Raman spectra of crystalline graphene, exhibiting the first-order Raman-allowed G-band. When graphene is bombarded by a low dose of Ar^+ ions ($10^{11}\,Ar^+/cm^2$), point defects are formed and the Raman spectra of the disordered graphene exhibit two new sharp features appearing at $1345\,cm^{-1}$ and $1626\,cm^{-1}$ for $E_{laser} = 2.41\,eV$, as seen in Figure 13.1b. These two features have been called the D and D′-bands, respectively, to denote disorder. These bands are dispersive, and they are observed at these special frequencies when excited with a 514 nm wavelength (2.41 eV) laser. Finally, when the periodic system is strongly disordered by a large ion dose ($10^{15}\,Ar^+/cm^2$), the Raman spectrum resembles the profile of the density of states for the higher-energy optical phonon branch (Figure 13.1c) [194, 195].

The basic description of disorder-induced peaks in the Raman spectra of sp^2 carbons comes from the double resonance model discussed in Chapter 12, and is associated with the following considerations. The requirement that only phonons at the center of the Brillouin zone are first-order Raman-allowed[1] ($q = 0$) by symmetry comes from momentum conservation, and momentum conservation is associated with translational symmetry. The effect of breaking the translational symmetry of

1) Not all zone-center phonons are Raman-allowed. Only phonons which behave like a symmetric second-order rank tensor, such as xy, $x^2 - y^2$, can be Raman-active modes (see Chapter 6).

Raman Spectroscopy in Graphene Related Systems. Ado Jorio, Riichiro Saito, Gene Dresselhaus, and Mildred S. Dresselhaus

ISBN: 978-3-527-40811-5

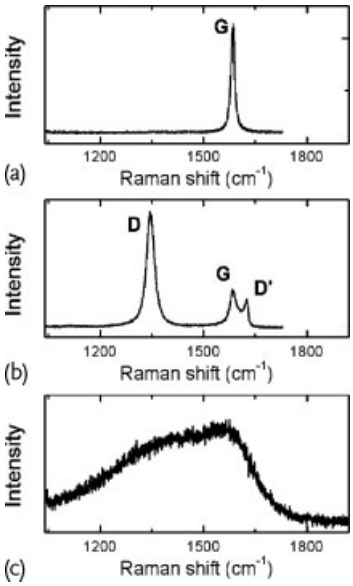

Figure 13.1 The first-order Raman spectrum of (a) crystalline graphene, (b) defective graphene, (c) and fully disordered single-layer graphene deposited on a SiO_2 substrate. These spectra are all obtained with $E_{laser} = 2.41$ eV [195].

crystals by introducing disorder into the lattice is the breakdown of momentum conservation, through the activation of phonons at interior k points of the Brillouin zone. Disorder-induced lattice distortions could also lead to a break down of other symmetry-based selection rules, thus also activating $q = 0$ phonons that are forbidden by the symmetry of the unperturbed crystal structure. For example, the out-of-plane TO phonon mode at 850 cm^{-1}, which is not Raman-active but is instead IR (infrared)-active, can be observed as a weak feature in Raman spectra in the presence of defects. Usually the effect of disorder on the Raman spectra of crystalline materials is a broadening of the Raman-allowed peaks (e. g., G and G′), the observation of new features (e. g., D and D′) related to symmetry forbidden scattering processes and, at high disorder levels, the observation of a phonon-density-of-states like spectra. These changes are all related to the turning on of new scattering processes by the progressive break-down of symmetry and by the introduction of new wave vectors to conserve momentum.

This chapter starts, in Section 13.1, with a brief taste of what would be a general quantum mechanical description of a defect-induced Raman effect. In Section 13.2 the defect-induced double resonance scattering processes are considered in detail, which describes, based on the electron and phonon dispersion relations, the frequencies of the disorder-induced Raman peaks and their dependence on E_{laser}. In Section 13.3, the D and D′ peak intensities are discussed, that is, how they evolve with increasing amounts of disorder. We address two systems, ion-bombarded graphene and nanographite, where disorder is represented by point

defects and by boundaries, respectively. In Section 13.4 we show that the zigzag edge has a special symmetry so that the D-band double resonance process is forbidden, although the D′ feature can be seen in the zigzag edge spectra. This is the first attempt [161] to use Raman spectroscopy to study the "atomic structure" of the defect and these results can be used to differentiate between zigzag and armchair graphene edges and grain boundaries. In sequence, Section 13.5 discusses specific details regarding the disorder found in one-dimensional carbon nanotubes, which includes multiple features in the G-band arising from disorder. Finally, in Section 13.6 a different concept is discussed, that is the effect that defects cause on Raman-allowed peaks, due to local electron and phonon energy renormalization. This effect has been observed by near-field optical measurements on the G′ feature in doped SWNTs and represents a new route for future research [191]. Section 13.7 summarizes the main points discussed in this chapter.

13.1
Quantum Modeling of the Elastic Scattering Event

For a full quantum description of the disorder-induced effect in the Raman spectra of SWNTs, it is necessary to calculate the Raman intensity $I(\omega, E_{\text{laser}})$ of a disorder-induced band, which is due to a double resonance scattering process [80], given by:

$$I(\omega, E_{\text{laser}}) = \sum_i \left| \sum_{a,b,c,\omega_{\text{ph}}} \frac{M_{\text{op}}(k, ic)\, M_{\text{def}}(-q, cb)\, M_{\text{ep}}(q, ba)\, M_{\text{op}}(k, ai)}{\Delta E_{ai}(\Delta E_{bi} - \hbar\omega_{\text{ph}})(\Delta E_{ci} - \hbar\omega_{\text{ph}})} \right|^2 \tag{13.1}$$

where $\Delta E_{ai} = (E_{\text{laser}} - (E_a - E_i) - i\gamma_{\text{r}})$ and γ_{r} denotes a broadening factor. Here subscripts i, a, b, and c, respectively, denote the initial state, the excited state, the first scattered state of an electron by a phonon, and the second scattered state of an electron by a defect. M_{op}, M_{ep} and M_{def} denote the electron–photon, electron–phonon and electron-defect scattering matrix elements, respectively. We use the fact that $E_b = E_c$ since the scattering from b to c is an elastic scattering process induced by the defect. Therefore, the new feature of Eq. (13.1) is the presence of the M_{def} matrix element, which describes the elastic scattering by defects. As previously discussed, in quantum mechanics the scattering processes can occur in different orders and, for example, the process in which elastic scattering occurs first in the double resonance process is also possible and has to be considered. For a given initial and final state i, all intermediate states are added before taking the square in Eq. (13.1).

An elastic electron scattering from electron state k to k' can be expressed by the matrix element [395]

$$M_{k'k} = \langle \Psi^{\text{c}}(k') | V | \Psi^{\text{c}}(k) \rangle \,, \tag{13.2}$$

in which $\Psi^c(k)$ is the conduction-band wavefunction of two-dimensional (2D) graphite (or monolayer graphene) at wave vector k, and $V = V_0 + V_{def}$ is the potential term of the Hamiltonian with crystal potential (V_0) and a defect perturbation potential (V_{def}). Here $\Psi(k)$ is expanded by the Bloch wavefunction Φ_s, and Φ_s is expressed in terms of the atomic wavefunction, $\phi(r - R_s)$ (see Chapter 2), thus giving:

$$M_{k'k} = \frac{1}{N_u} \sum_{s,s'} C^*_{s'}(k') C_s(k) \sum_{R_s, R_{s'}} \exp\left(-ik'R_{s'} + ikR_s\right) V_{s's} \,, \tag{13.3}$$

where $V_{s's}$ is the atomic matrix element of V defined by $\langle \phi(R_{s'})|V|\phi(R_s)\rangle$. When $V = V_0$, then $V_{s's}$ depends only on $R_{s'} - R_s$, and also $M_{k'k}$ has a nonvanishing value only for $k' = k$[2] which implies crystal momentum conservation. If we remove a carbon atom from the site s', the atomic tight-binding matrix elements $\langle \phi(R_{s'})|V|\phi(R_s)\rangle$ containing s' become zero and then elastic scattering from k to k' occurs. When we consider the tight-binding method within the nearest neighbor interaction, then the tight-binding γ_0 parameter becomes zero for the atoms that are nearest neighbors to the site s'. This means that we add $-\gamma_0$ parameters for the three nearest s sites as tight-binding parameters for V_{def}, and Eq. (13.3) for $k' \neq k$ then becomes:

$$M_{k'k} = -\frac{\gamma_0}{N_u} C^*_{s'}(k') C_s(k) \sum_{R_s} \exp\left(-ik'R_{s'} + ikR_s\right) \,, \tag{13.4}$$

where a summation on R_s is taken only for the three nearest neighbor atoms to the s' atom.

However, this expression for $M_{k'k}$ is too simple and a fundamental correction to this expression is necessary. Since the impurity potential for the missing atom ($-\gamma_0$) is of the same order as for the tight-binding parameter of the electronic structure (γ_0), the matrix element cannot be expressed within the lowest order of perturbation theory and we must consider higher-order terms. In order to obtain such higher-order terms, we consider the correction to the wavefunction $\Psi^c(k)$ due to the presence of such defects. In fact, the perturbation to $\Psi^c(k)$ as an electron is scattered around the defect mixes many $\Psi^c(k')$ wave functions for different wave vectors with $\Psi^c(k)$ for $k' \neq k$. The perturbed wavefunction Φ in the presence of an impurity potential V_{def} which is defined by the difference between the unperturbed potential and the potential after adding the defect, is given by:

$$\Phi(k) = \Psi^c(k) + \sum_{k'} \frac{\langle \Psi^c(k')|V_{def}|\Psi^c(k)\rangle}{E(k') - E(k) + i\gamma} \Psi^c(k') \,, \tag{13.5}$$

where γ is a broadening factor due to the finite lifetime of carriers due to the defect scattering (introduced by the uncertainty relation). It is noted that k in $\Phi(k)$ no longer has the meaning of "as a function of k" but rather is modified by the

2) The umklapp scattering process $k' = k + G$ (where G is a reciprocal lattice vector) also occurs.

correction to $\Psi^c(k)$. Thus, when we put Eq. (13.5) into Eq. (13.2) to redefine $M_{k'k}$, we now obtain:

$$\begin{aligned} M_{k'k} &\equiv \langle \Phi(k')|V_{\text{def}}|\Phi(k)\rangle \\ &= \langle \Psi^c(k')|V_{\text{def}}|\Psi^c(k)\rangle \\ &\quad + \sum_{k''} \frac{\langle \Psi^c(k')|V_{\text{def}}|\Psi^c(k'')\rangle\langle \Psi^c(k'')|V_{\text{def}}|\Psi^c(k)\rangle}{E(k'') - E(k) + i\gamma} \,. \end{aligned} \tag{13.6}$$

Equation (13.6) then gives the next order correction to the matrix element for elastic scattering. Since we consider the elastic scattering $E(k'') = E(k)$, in Eq. (13.6), the value of γ can not be neglected. Using the Fermi Golden rule for a second-order time-dependent perturbation, γ is proportional to the sum of $|M_{k'k}|^2$ which is inversely proportional to the lifetime of the k state, and the γ values are determined self-consistently. When we substitute $\Phi(k')$ for $\Psi^c(k')$ in the last term of Eq. (13.5), we can iteratively obtain the expansion of the perturbation series. The corresponding $M_{k'k}$ is defined iteratively. An infinite series for this expansion of the scattering matrix elements is called the *T-matrix* [396, 397]. Here we do not go into detail regarding the quantum theory of the T-matrix, but rather we point out that the calculation of the T-matrix is necessary for discussing elastic scattering.

An important fact is that the Fourier transform of $V_{\text{def}}(r)$ to q space to obtain $V_{\text{def}}(q)$ determines the range of the defect potential. When V_{def} is a short-range potential such as a point defect, a dominant contribution to $V_{\text{def}}(q)$ comes from a large range of q values since intervalley scattering from the K to K' valley (or vice versa) is important. On the other hand, when V_{def} is a long-range potential, then intravalley scattering is dominant. In the case of intravalley scattering, then backward scattering is absent for the quantum interference effect, which is significant in the case of single-wall carbon nanotubes [396, 397].

Figure 13.2 shows the calculated spectral D-band Raman intensity for a nanoribbon with an armchair edge, for three different laser energies of 1.90 eV (solid line), 2.30 eV (dashed line) and 2.70 eV (dotted line), as described in [395]. The defects here are the edges with an armchair atomic structure, and the sp^2 periodicity is broken by the missing atoms at the edge bonds. The elastic matrix elements are taken in the calculation at the lowest order of $M_{k'k}$ as in Eq. (13.2), which is here given analytically [395]. When the armchair edge exists in the direction of x, then the k_x component of k conserves momentum, while k_y changes its sign (by reflection), which corresponds to intervalley scattering. The $M_{k'k}$ matrix element for the zigzag edge does not contribute to intervalley scattering,[3] which means the D-band should be absent when measuring zigzag edges, as observed experimentally (see Section 13.4).

When comparing the results in Figure 13.2 with experiment, the frequency dependence of the D-band feature on E_{laser} is well described (see inset to Figure 13.2). The D-band peak come from the iTO phonon dispersion branch near the K point for which $q \approx 2k$, as dictated by the double resonance process [159, 160], and this

3) In the case of the zigzag edge, k_x changes its sign and this corresponds to intravalley scattering (K to K, or K' to K').

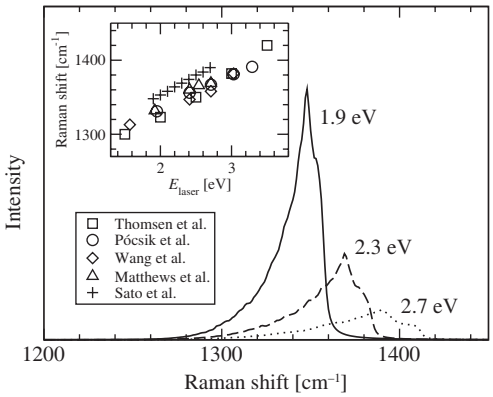

Figure 13.2 The calculated Raman spectra of the D-band for $E_{laser} = 1.90$ eV (solid line), 2.30 eV (dashed line), 2.70 eV (dotted line) considering a nanoribbon with an armchair edge [395]. The inset shows a comparison of ω_D vs. E_{laser} between various works [159, 395, 398–400], where crosses represent the calculated results discussed here [395].

topic is discussed more fully in Section 13.2. However, an accurate description of the scattering intensity behavior (e. g., its dependence on both E_{laser} and ribbon width, and the matrix element dependence on q generating an asymmetric D-band lineshape) has still not been fully achieved. This is not only because the T-matrix was not considered correctly, but because other aspects such as the phonon coherence length and the resonance window width γ have not been considered self-consistently. Therefore, while the present section gives a taste on how to fully treat the process quantum mechanically, and indicates an accurate description of disorder-induced Raman features, for an accurate quantum mechanical description of the Raman intensities, more work is still needed.

13.2
The Frequency of the Defect-Induced Peaks: the Double Resonance Process

Defects break the momentum conservation requirement $q = 0$ for the first-order Raman-allowed phonons, so that, in principle, any scattering event involving phonons in the interior of the Brillouin zone ($q \neq 0$), would then be allowed. However, as discussed in Chapter 12, in sp^2 carbon materials the resonant electron–phonon scattering processes connecting real electronic states (see Figure 13.3a) minimize the denominators in Eq. (13.1), that is, these resonant processes are privileged and have much higher probabilities, so that the spectra are dominated by the double resonance scattering processes. While momentum conservation in a perfect lattice can only be fulfilled by $q = 0$ phonons or two-phonon scattering processes with $q - q = 0$, as discussed in Chapter 12, in the presence of disorder

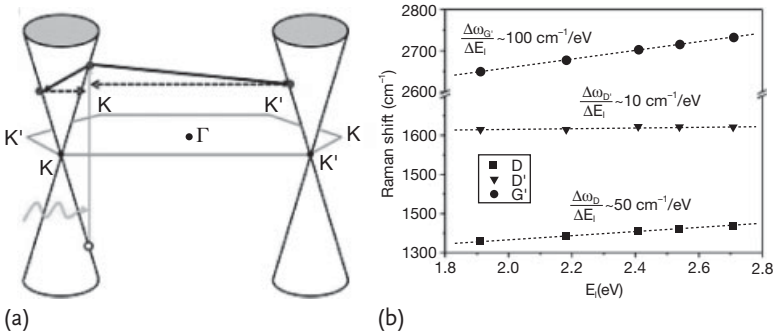

Figure 13.3 (a) Schematics showing the electronic dispersion near the Fermi level at the *K* and *K′* points in the hexagonal Brillouin zone of graphene. The light-induced electron–hole formation is indicated by a gray arrow. The two resonant electron–phonon scattering processes associated with the D (intervalley) band and the D′ (intravalley) band are indicated by the black arrows. The dashed arrows indicate elastic scattering induced by defects. (b) Laser energy dependence or dispersion of the frequency of the D, D′ and G′-bands [394].

the momentum conservation can be satisfied through an elastic scattering process by a defect, as represented by dashed arrows shown in Figure 13.3a.

Therefore, the frequencies of the defect-induced peaks are well explained by the double resonance processes discussed in Chapter 12, although some special details have to be taken into account. For example, from a frequency analysis, we see that both the D and D′-band scattering events shown in Figure 13.3 are the one-phonon processes that are related to the two-phonon processes observed at $2700\,\mathrm{cm}^{-1}$ (G′ $\sim$ 2D) and at $3240\,\mathrm{cm}^{-1}$ (G″ $\sim$ 2D′) in Figure 4.14. The dispersions of the frequencies of the D, D′ and G′-bands are shown in Figure 13.3b by plotting their frequency dependence on E_{laser}. The slope associated with the G′-band is about $100\,\mathrm{cm}^{-1}$/eV and is two times larger than the slope of the D-band ($50\,\mathrm{cm}^{-1}$/eV). The D′-band also exhibits a weak dispersive behavior, the slope being about $10\,\mathrm{cm}^{-1}$/eV [394]. However, there is no exact matching between the D and G′-bands (i. e., $\omega_{G'} \neq 2\omega_{D}$) because their physical processes have some differences. As discussed in Section 12.2.1, different q vectors give rise to different double resonance processes in the Stokes (S) and anti-Stokes (aS) processes ($q_{S} \neq q_{aS}$). The same applies to the disorder-induced bands and more: within a one-phonon Stokes double resonance process, different wave vectors q will be introduced if we consider the elastic scattering taking place either before or after the inelastic phonon scattering (see Figure 13.4) [80, 367].

The D and D′-bands are not the only disorder-induced one-phonon peaks in the Raman spectra for disordered sp^2 materials (see Figure 12.10). Similar to the two-phonon processes discussed in Section 12.3, which can occur through any combination or overtone of the six dispersive phonon energy branches in graphene, the disorder-induced Raman frequencies can be related to any of the six phonon branches of 2D graphite with the appropriate wave vector which fulfills the double resonance condition. The intravalley and intervalley double resonance processes

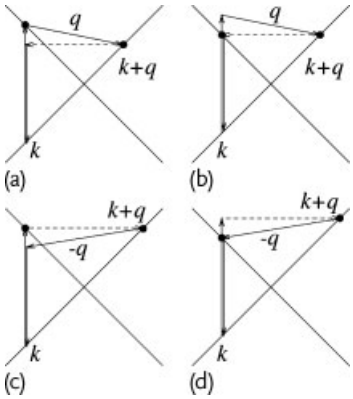

Figure 13.4 Four different one-phonon intravalley second-order double resonance Stokes processes. For each process, the dashed lines denote an elastic scattering process and black dots are shown for the resonant points. For the two-phonon second-order processes, the dashed line of each figure is changed to be an inelastic phonon emission process and thus only the (a) and (d) processes are possible for two-phonon scattering processes [160] (see the (a) and (d) panels in Figure 12.3).

are mediated by phonons near the Γ and K (or K') points, respectively, and we can change both the resonant k and q values by changing E_{laser}, as determined by Eq. (12.8). Thus by using electronic structure information, we can determine the phonon dispersion relations around the K and the Γ points, by considering intervalley and intravalley processes, respectively. For both intervalley and intravalley processes, the fitting between the observed Raman frequencies and the dispersion relations depend upon the different possibilities for second-order double resonance processes. Four of them are exemplified in Figure 13.4 for the intravalley Stokes Raman scattering process, as is for example pertinent to the D′ band.

Figure 13.5a plots the E_{laser} dependence of the disorder-induced double resonance peaks, as obtained considering a linear electronic dispersion (see Chapter 2) and the phonon dispersion in Figure 13.5b. The lower horizontal axis of Figure 13.5a correlates the E_{laser} values with the phonon wave vectors q indicated in the upper horizontal axis for Γ to $K/4$ and for $3K/4$ to K. These q values are also shown in Figure 13.5b and are related to intravalley and intervalley processes obeying $q \approx 2k$ (see Eq. (12.8)) [160]. It is noted that the linear relationship between E_{laser} and k, and consequently between E_{laser} and q is valid for $E_{\text{laser}} < 3.0\,\text{eV}$ (see Figure 2.10 in Chapter 2), and the vertical dotted lines in Figure 13.5b show limits for the q wave vectors imposed by $E_{\text{laser}} < 3.0\,\text{eV}$. By comparing Figure 13.5a,b, it is easy to correlate the double resonance peaks with the six different phonon branches in graphite. Solid and open circles correspond to the phonon modes around the K and the Γ points, respectively. Nondispersive features are also seen in Figure 13.5a, and they come from the $q \approx 0$ double resonance condition (see Eqs. (12.6) and (12.7), and related text).

Finally, by using the E_{laser} vs. q relations given in Figure 13.5a, we can take experimental values from several published papers giving Raman frequencies observed

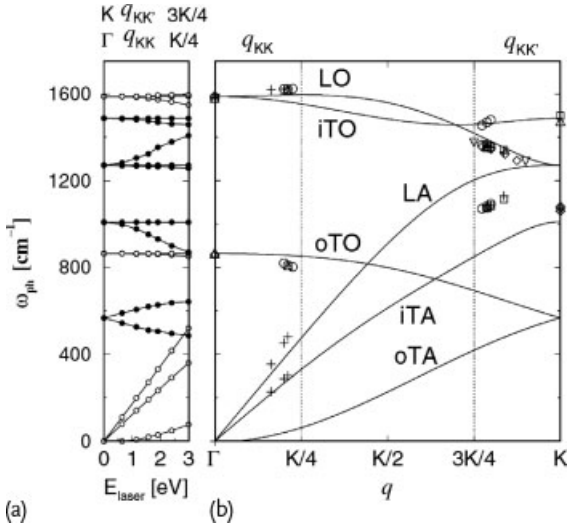

Figure 13.5 (a) Calculated Raman frequencies for the double resonance condition in 2D graphite as a function of E_{laser} (bottom horizontal axis) and the corresponding q vector along Γ-K (top horizontal axis). Solid and open circles correspond to phonon modes around the K and the Γ points, respectively. The q_{KK} vectors from Γ to $K/4$ are shown by open circles and the $q_{KK'}$ vectors from $3K/4$ to K are shown by solid circles. (b) The six graphite phonon dispersion curves (lines) and experimental Raman observations (symbols) consistent with double resonance theory [160].

using different laser lines for various sp^2 carbons (e. g., Figure 12.10) and plot all these data points in Figure 13.5b. Notice that in the Raman spectra there is no information on whether the peak comes from an intravalley or intervalley process, and on obeying the $q \approx 0$ or $q \approx 2k$ resonance conditions. We choose among these possible scattering assignments by considering where the experimental data would best fit in the phonon dispersion in Figure 13.5b. The discrepancies can be due to wrong scattering assignments or inaccurate phonon dispersion relations. In fact, these double resonance peak assignments have been largely used to improve the theoretical modeling of phonons in sp^2 nanocarbons [366].

13.3 Quantifying Disorder in Graphene and Nanographite from Raman Intensity Analysis

As discussed in Section 13.2, the frequencies of the disorder-induced features in the Raman spectra for sp^2 carbons are well-explained by the double resonance model. What remains to be established for making Raman spectroscopy a powerful tool to characterize disorder in sp^2 materials is how to relate specific defects to their corresponding disordering processes, and how to obtain quantitative information about the amount of such defects in the lattice. As briefly discussed in Section 13.1, more experimental and theoretical work is still needed for an accurate

quantum mechanical description of disorder-induced Raman processes. However, some work has already been done and phenomenological models have been developed, as described below.

Extensive work in the field of amorphous carbon leads to a description of the amorphization trajectory for carbon materials (see Figure 4.7c in Section 4.4.1). However, to achieve a quantitative description of these phenomena, the effects of disorder on the electron and phonon properties have to be probed in both momentum space (*k*-space) and real space (*r*-space), which means Raman spectroscopy has to be combined with microscopy experiments. For example, transmission electron microscope (TEM) or scanning tunneling microscopy (STM) can characterize disorder in the crystal *r*-space by probing the local surface density of electronic states, with atomic-level resolution. Simultaneous in-situ TEM and Raman measurements are, in principle, possible. However, a special experimental set up and special sample preparation methods would be needed. Usually, STM and Raman spectroscopy cannot be easily correlated with each other, since optical spectroscopy probes a volume that is limited by the light penetration depth, while STM is mostly sensitive to surfaces. In this context, the possibility of exfoliating graphite to pull out a single graphene sheet, provides an ideal situation in which microscopy and spectroscopy can be correlated to probe disorder effects in both *r*-space and *k*-space. The initial efforts in this research direction are now discussed.

13.3.1
Zero-Dimensional Defects Induced by Ion Bombardment

The controlled use of ion implantation to study defects in sp^2 carbons is a well established technique [401]. These experiments are normally carried out as a function of ion dose and for different ion species and different ion energies. Low mass ions at low ion fluence introduce point defects. Increasing the ion dose causes an increasing density of point defects and eventually causes the damaged regions to overlap. In this section we discuss effects from Ar^+ implantation as a function of ion dose and the resulting damage to HOPG [402] and graphene [194, 195].

Consecutive Ar^+ ion bombardment and Raman spectroscopy experiments were performed on monolayer graphene samples [194]. Low energy ions (90 eV), experimentally confirmed to barely exceed the threshold value for the displacement of surface C atoms, were used to produce structural defects in the graphene layer, thereby avoiding cascade effects.[4] The bombardment ion doses span the typical values that are used for ion implantation studies, starting with 10^{11} Ar^+ impacts per cm^2, which corresponds to one defect per 4×10^4 C atoms, and going up to 10^{15} Ar^+/cm^2, denoting the onset of full disorder in graphene. STM images show that for up to 10^{12} Ar^+/cm^2, the ion bombardment-induced defects are isolated from each other, with each defect causing a rather large disordered area in the STM images ($\sim$ 1 nm radius). Near a 10^{13} Ar^+/cm^2 dose, the disordered areas start to

4) Cascade effects are effects whereby a scattered C atom with a large energy hits another C atom iteratively. Similar phenomena can be seen in the chain reaction of dominos.

coalesce and the surface exhibits a mixture of ordered and disordered regions. At a 10^{14} Ar^+/cm^2 dose and above, the hexagonal crystalline pattern can no longer be observed by probing the local density of electronic states by STM. Analysis of the STM images at each ion dose gives the defect concentration from which we can extract the average distance between defects, $L_D = \sigma^{-1/2}$, where σ is the density of defects. Therefore, the σ and L_D values can be obtained from the STM images by the direct counting of defects [194]. For the highest ion doses of 10^{15} Ar^+/cm^2, when the effect of defects start to coalesce, we consider that the defect density increases linearly with bombardment time.

Figure 13.6 shows the Raman spectra of a graphene monolayer subjected to the ion bombardment procedure as described above. From the pristine sample (bottom spectrum) to the lowest bombardment dose in Figure 13.6 (10^{11} Ar^+/cm^2), the D-band process is activated, showing a very small intensity relative to the G peak. Within the bombardment dose range 10^{11}–10^{13} Ar^+/cm^2, the intensities of the disorder peaks increase. A second disorder-induced peak around $\sim 1620\,cm^{-1}$ (the D′-band) also becomes evident, but we do not focus on this feature here. Above 10^{13} Ar^+/cm^2, the Raman spectra start to broaden significantly and end up exhibiting a profile similar to the graphene phonon density of states (PDOS). From the 10^{14} (top spectrum) to 10^{15} Ar^+/cm^2 (not shown) dose, the Raman scattering response develops its PDOS-like profile, showing a lineshape broadening with no change in peak frequencies.

Quantifying the development of disorder in a graphene monolayer can be achieved by plotting the I_D/I_G data as a function of the average distance between defects L_D, as shown in Figure 13.7. The I_D/I_G ratios are here obtained

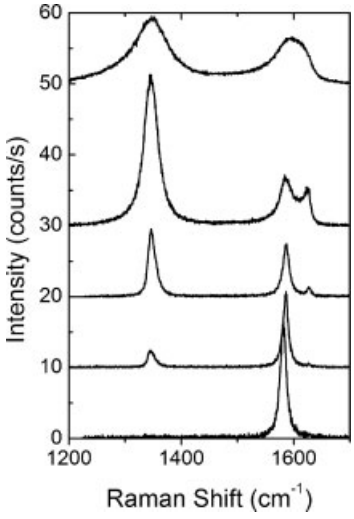

Figure 13.6 Evolution of the first-order Raman spectra using a $\lambda = 514\,nm$ laser of a graphene monolayer sample deposited on an SiO_2 substrate, subjected to Ar^+ ion bombardment. The ion doses are from the bottom to the top, 0, 10^{11}, 10^{12}, 10^{13} and 10^{14} Ar^+/cm^2. The spectra in this figure are also displaced vertically for clarity [194].

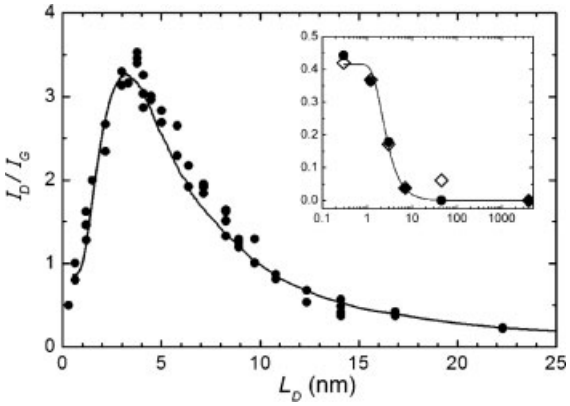

Figure 13.7 The I_D/I_G data points from three different monolayer graphene samples as a function of the average distance L_D between defects, induced by the ion bombardment procedure. The solid line is a modeling of the experimental data with Eq. (13.7). The inset shows a plot of I_D/I_G vs. L_D on a log scale for two samples: (i) a $\sim$ 50-layer graphene sample; (ii) a 2 mm-thick HOPG sample, whose measured values are here scaled by $(I_D/I_G) \times 3.5$ [194].

by considering the peak intensity at the fixed D-band (1345 cm^{-1}) and G-band (1585 cm^{-1}) frequencies. The I_D/I_G ratio has a nonmonotonic dependence on L_D, increasing initially with increasing L_D up to $L_D \sim 3.5$ nm where I_D/I_G has a peak value, and then decreasing for $L_D > 3.5$ nm. This result is similar to the proposed amorphization trajectory for graphitic nanocrystallites (see Section 4.4.1), and such a behavior suggests the existence of two disorder-induced competing mechanisms contributing to the Raman D-band. These competing mechanisms are the basis for a phenomenological model for the L_D dependence of I_D/I_G that is now described (Section 13.3.2).

13.3.2
The Local Activation Model

The results in Figure 13.7 are modeled by assuming that a single impact of an ion on the graphene sheet causes modifications on two length scales, here denoted by r_A and r_S (with $r_A > r_S$), which are the radii of two circular areas measured from the impact point (see Figure 13.8). Within the shorter radius r_S, structural disorder from the impact occurs. We call this the structurally-disordered or *S*-region. For distances larger than r_S but shorter than r_A, the lattice structure is preserved, but the proximity to a defect causes a mixing of Bloch states near the K and K' valleys of the graphene Brillouin zone, thus causing a break-down of the selection rules, and leading to an enhancement of the D-band. We call this the defect activated or *A*-region. In qualitative terms, an electron–hole excitation will only be able to "see" the structural defect if the electron–hole pair is created sufficiently close to the defect and if the excited electron (or hole) lives long enough for the defective

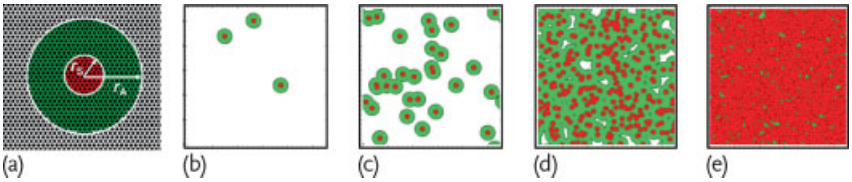

Figure 13.8 (a) Definition of the "activated" *A*-region (darkest gray) and "structurally disordered" *S*-region (dark gray). The radii are measured from the impact point which is chosen randomly in our simulation. Parts (b–e) shows 55 nm × 55 nm portions of the graphene simulation cell, with snapshots of the structural evolution of the graphene sheet for different defect concentrations: (b) $10^{11}\,\mathrm{Ar}^+/\mathrm{cm}^2$; (c) $10^{12}\,\mathrm{Ar}^+/\mathrm{cm}^2$; (d) $10^{13}\,\mathrm{Ar}^+/\mathrm{cm}^2$; (e) $10^{14}\,\mathrm{Ar}^+/\mathrm{cm}^2$, like in Figure 13.6 [194].

region to be probed by Raman spectroscopy. If the Raman scattering process occurs at distances larger than $\ell = r_A - r_S$ from the defective region, the wave vector k is a good quantum number for analyzing the scattering selection rules and those regions that remain well ordered will only contribute significantly to the G-band. Our phenomenological model for the I_D/I_G ratio is given as a function of the average distance between two defects, L_D:

$$\frac{I_D}{I_G}(L_D) \propto I_D(L_D) = C_A f_A(L_D) + C_S f_S(L_D)\,, \tag{13.7}$$

where I_G is considered as constant (independent on L_D), and f_A and f_S are simply the fractions of the A and S areas in the sheet, respectively, with respect to the total area. Although both the A and S regions can break momentum conservation, giving rise to a D-band, the A-regions will contribute most strongly to the D-band, while the S-regions will make less contribution to the D-band due to the breakdown of the lattice structure itself.

We now describe stochastic simulations (see Figure 13.8b–e) used to implement the phenomenological model for the I_D/I_G ratio. The structurally-disordered (S) region is shown in light gray in Figure 13.8a and the activated (A) region is shown in dark gray in Figure 13.8a. The structural evolution of a graphene sheet under ion bombardment was simulated by randomly choosing a sequence of impact positions on a (50 nm × 50 nm) sheet. The following set of rules for each event was defined: (1) pristine regions (white area in Figure 13.8b–e) may turn into S (light gray) or A (dark gray) regions, depending on the proximity to the impact point; (2) similarly, A-regions may turn into S (light gray); (3) S-regions always remain S regions. Then, the initially pristine sheet evolves, as the number of impacts increase, to become mostly activated, leading to an increase of the D-band, and later the mostly structurally-disordered regions become increasingly widespread, leading to a decrease of the D-band. Snapshots of this evolution are shown in Figure 13.8b–e for the same argon ion concentrations as in Figure 13.6. The stochastic simulations of the bombardment process, with the impact points for the ions chosen at random, combined with Eq. (13.7) with parameters $C_A = 4.56$, $C_S = 0.86$, $r_A = 3\,\mathrm{nm}$ and $r_S = 1\,\mathrm{nm}$, give the full line curve in Figure 13.7, which is in excellent agreement with the experimental results (points) in this figure [194].

The nonmonotonic behavior in Figure 13.7 can be understood by considering that, for low defect concentrations (large L_D), the total area contributing to scattering is proportional to the number of defects, giving rise to a $I_D/I_G = (102 \pm 2)/L_D^2$ dependence that works well for $L_D > 2r_A$. Upon increasing the defect concentration, the activated regions start to overlap and these regions eventually saturate. The D-band intensity then reaches a maximum and a further increase in the defect concentration decreases the D-band intensity because the graphene sheet starts to be dominated by the structurally-disordered areas.

The length scale $r_S = 1\,\text{nm}$, which defines the structurally-disordered area, is in perfect agreement with the average size of the disordered structures seen in the STM images. This parameter should not be universal, but it is specific to the bombardment process. The Raman relaxation length ℓ for the defect-induced resonant Raman scattering in graphene for a laser energy of 2.41 eV, is found to be $\ell = r_A - r_S = 2\,\text{nm}$.[5] The C_A parameter in Eq. (13.7) is a measure of the maximum possible value of the I_D/I_G ratio in graphene, which would occur in a hypothetical situation in which $K - K'$ wave vector mixing would be allowed everywhere, but no damage would be made to the hexagonal network of carbon atoms. C_A should then be defined by the electron–phonon matrix elements, and the value $C_A = 4.56$ is then in rough agreement with the ratio between the electron–phonon coupling for the iTO phonons evaluated between the Γ and the K points [366]. The C_S parameter is the value of the I_D/I_G ratio in the highly disordered limit, which has not yet been addressed theoretically.

Finally, for practical use, it is important to have an equation relating I_D/I_G to L_D, and such an equation can be obtained by solving rate equations for the bombardment process (see problem set). The entire regime ($0 \rightarrow L_D \rightarrow \infty$) can be fitted using:

$$\frac{I_D}{I_G} = C_A \frac{r_A^2 - r_S^2}{r_A^2 - 2r_S^2}\left[\exp\left(\frac{-\pi r_S^2}{L_D^2}\right) - \exp\left(\frac{-\pi(r_A^2 - r_S^2)}{L_D^2}\right)\right] + C_S\left[1 - \left(\frac{-\pi r_S^2}{L_D^2}\right)\right]. \tag{13.8}$$

Fitting the data in Figure 13.7 with Eq. (13.8) gives $C_A = (4.2 \pm 0.1)$, $C_S = (0.87 \pm 0.05)$, $r_A = (3.00 \pm 0.03)\,\text{nm}$ and $r_S = (1.00 \pm 0.04)\,\text{nm}$, also in excellent agreement with experiment and consistent with the parameters obtained within the computational modeling [194].

The present model provides a method to accurately quantify the density of defects σ or, equivalently, the average distance between defects ($L_D = \sigma^{-1/2}$) in graphene. Before the defects start to coalesce ($L_D > 6\,\text{nm}$ in the present case), the expected behavior occurs, that is, $I_D/I_G = A/L_D^2$, where $A = (102 \pm 2)\,\text{nm}^2$ was found. When the defects start to coalesce there is a competition between two disorder mechanisms, and Eq. (13.8) can be used for a quantitative analysis to determine the relative importance of each mechanism. The present results discussed

5) Here we discuss the relaxation length for the excited electron, and this should not be confused with the relaxation length for the phonons.

for graphene are similar to what has been observed in ion bombarded HOPG [402], although some details are different. First, for HOPG a larger G-band is always observed due to the contribution from the undisturbed under-layers. Second, for graphene, above 10^{15} Ar^{+}/cm^{2}, the spectra show a decreased intensity, indicating full amorphization or partial sputtering of the graphene layer. For HOPG, above 10^{15} Ar^{+}/cm^{2}, I_D/I_G saturates and no further change is observed in the Raman spectra because of the large number of layers that have been amorphitized and/or sputtered. This behavior is seen in the inset to Figure 13.7, which shows the I_D/I_G evolution for two HOPG samples of different thicknesses. Despite differences in absolute values, which depend on the number of undisturbed under-layers (the diamond data in the inset to Figure 13.7 coming from a thicker HOPG sample was scaled by $\times 3.5$), the I_D/I_G values increase and saturate when increasing the ion dose.

A study of the I_D/I_G evolution as a function of L_D depending on the number of layers N has also been developed [195]. The I_D/I_G behavior was observed to scale with N, clearly demonstrating the lower energy ions (90 eV) used in the experiment were not able to do cascade effects, but the process is limited generally to one defect per bombarding ion. For few-layer graphene samples ($N = 1, 2, 3$), the normalized evolution of I_D/I_G increases with increasing the number of defects (increasing the "activated area"[194]), and further saturates and decreases. This decrease is due to the take-over of the activated area by the "disordered area", as introduced previously for 1-LG [194]. However, the decrease in I_D/I_G for larger ion doses is less evident the larger the N. For many-layers graphene ($\sim$ 50 and higher), the normalized evolution of I_D/I_G with increasing number of defects is a monotonic increase, since there are always more graphene layers to be bombarded.

In summary, this section gives a clear picture of the basic mechanisms behind the evolution of the disorder-induced D-band for point defects, which is given by a competition between the structurally-damaged area, and the D-band-activated area relative to the total area. Since this is basically a geometric interplay, different results will be obtained when moving from the "zero-dimensional" defects caused by ion bombardment in graphene, and the "one-dimensional" defects represented by the boundaries of a nanocrystalline graphene sample or a graphite crystal. These nanocrystalline systems actually represent an extensively studied system, usually formed by the annealing of diamond-like carbon films formed by sputtering [168], and are discussed in the next section.

13.3.3
One-Dimensional Defects Represented by the Boundaries of Nanocrystallites

In 1970, Tuinstra and Koenig [148, 149] performed systematic Raman and X-ray diffraction studies of many graphitic samples with different in-plane crystallite sizes L_a. These authors concluded that the ratio of the D and G-band intensities (I_D/I_G) is inversely proportional to L_a, which was determined from the width of the X-ray diffraction peaks. After this pioneering work, the ratio I_D/I_G was used for many years to estimate L_a in disordered carbon materials. Knight and White [403]

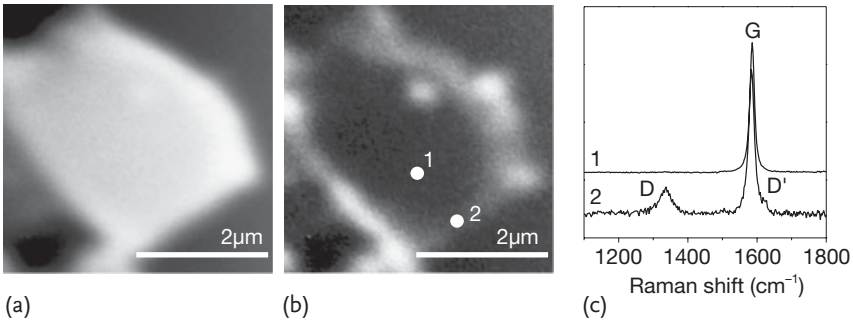

Figure 13.9 (a) G-band and (b) D-band confocal (300 nm resolution) Raman images of a graphite crystallite deposited on a glass substrate. In (c) the Raman spectra obtained in regions 1 and 2 (white circles depicted in panel (b)) are shown. The laser excitation comes from a HeNe ($\lambda = 633$ nm) laser using an experimental setup described in [394].

later summarized the Raman spectra of various graphitic systems measured using the $\lambda = 514.5$ nm ($E_{\text{laser}} = 2.41$ eV) laser line, and they derived an empirical expression which allows the determination of L_a from the (I_D/I_G) ratio [403]. Later, a general formula was developed giving I_D/I_G vs. L_a for nanographite systems for any excitation laser energy in the visible range, as presented below [404].

Figure 13.9a,b show two confocal Raman images of a 6 nm-high HOPG crystallite deposited on a glass substrate. Figure 13.9a shows a Raman image of the crystallite, obtained by plotting the spatial dependence of the G-band intensity, while in Figure 13.9b the spatial dependence of the intensity of the disorder-induced D-band is shown and here the boundary of the crystallite is highlighted. Figure 13.9c shows two Raman spectra, one taken at an interior point of the crystallite, and the other at the edge. It is clear from Figure 13.9a–c that the G-band intensity is uniform over the whole graphite surface, while the D-band intensity is localized where the crystalline structure is not perfect, mostly at the edges of the crystallite. Notice also that the D-band intensity varies from edge to edge, and this D-band intensity is dependent on the light polarization direction and the atomic structure at the edge, as is discussed in Section 13.4.

For evaluation of the I_D/I_G dependence on the crystallite dimensions, one can consider a square of side L_a, for which the intensity of the G-band will vary as $I_G \propto L_a^2$. The intensity of the D-band will, however, depend on the width δ of the "border" where the D-band is activated, given by $I_D \propto L_a^2 - (L_a - 2\delta)^2$. The intensity ratio will then be given by:

$$\frac{I_D}{I_G} = \alpha \left[4 \left(\frac{\delta}{L_a} - \frac{\delta^2}{L_a^2} \right) \right] , \tag{13.9}$$

where α is dependent on the appropriate matrix elements [394].

In the limit $L_a \gg \delta$, Eq. (13.9) can be simplified to yield the famous Tuinstra–Koenig relation

$$\frac{I_D}{I_G} = C(E_{\text{laser}})/L_a , \tag{13.10}$$

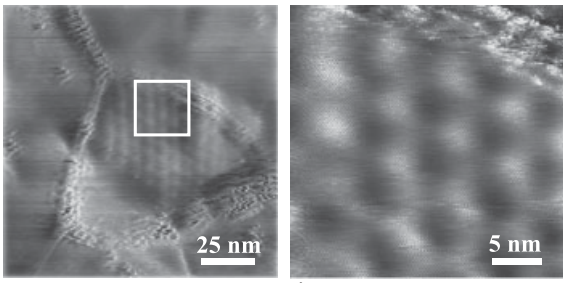

Figure 13.10 Scanning tunneling microscopy (STM) images with atomic resolution obtained from the surface of a nanographite crystallite of a sample with $L_a = 65\,\text{nm}$. (a) A Moire pattern at the crystallite surface is observed. (b) Magnification of the region delineated by the white square in part (a) [405].

where the values of the empirical constant $C(E_{\text{laser}})$ change from paper to paper in the literature. One could then expect that, once the relaxation length and matrix element ratio were measured for the D-band scattering in ion-bombarded graphene (Section 13.3.2), these values could just be transferred here to obtain α and δ. However, these factors depend on the structurally-disordered area (S_S), which is not well defined for the nanographite. Figure 13.10 shows two scanning tunneling microscopy (STM) images with atomic resolution obtained from the surface of a crystallite in a sample with $L_a = 65\,\text{nm}$. The atomic arrangement of the carbon atoms observed in these pictures indicates that the samples are formed by nanographitic crystallites, but with a clearly disordered grain boundary between crystallites [405]. Variability associated with these grain boundaries may be responsible for the different I_D/I_G vs. L_a results observed in the literature.

Furthermore, the empirical constant $C(E_{\text{laser}})$ has been known to depend on E_{laser} since 1984 [152], but $C(E_{\text{laser}})$ has been quantitatively developed only more recently [404], using experimental results from nanographites with different L_a values prepared from diamond-like carbon (DLC) films heat treated at different temperatures T_{htt} [404]. Before heat treatment, the sp^3 and sp^2 carbon phases coexist in the samples, but the sp^3 phases completely disappear for $T_{\text{htt}} > 1600^\circ\text{C}$ [406]. STM images of the samples obtained at different heat treatment temperatures $T_{\text{htt}} \geq 1800^\circ\text{C}$ show that these samples correspond to aggregates of nanographite crystallites, and show increasing L_a with increasing T_{htt}. The evolution of the (100) X-ray diffraction peak obtained using synchrotron radiation, for the samples heat treated at different T_{htt} also give a measure of the crystallite sizes, by evaluating L_a from the Scherrer relation $L_a = 1.84\lambda/\beta\cos\theta$, where λ is the synchrotron radiation wavelength (0.120 nm), θ is the position of the (100) diffraction peak, and β is the half-height width of the (100) peak of graphite in 2θ (rad) units [404]. The mean crystallite sizes obtained by X-ray diffraction range from 20 to 500 nm in size, and the X-ray values are in good agreement with the L_a values obtained directly from the STM images [376, 404, 405].

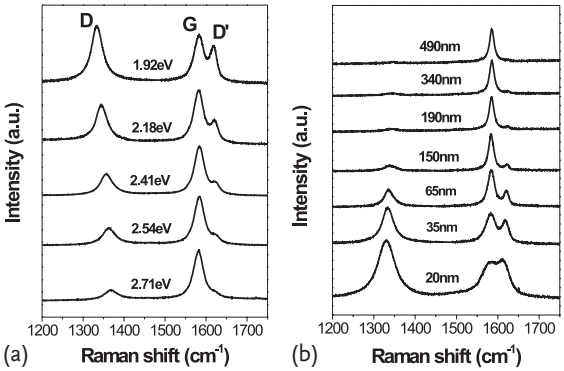

Figure 13.11 The first-order Raman spectra of (a) the nanographite sample heat treated at 2000°C ($L_a = 35$ nm), for five different laser energy values (1.92 eV, 2.18 eV, 2.41 eV, 2.54 eV, and 2.71 eV). (b) Nanographite samples with different crystallite sizes L_a (in mm) using 1.92 eV laser excitation energy [404].

Shown in Figure 13.11a are results from Raman scattering experiments performed at room temperature with different E_{laser} values, showing spectra of the D, G, and D′-bands for the $T_{\text{htt}} = 2000°\text{C}$ sample ($L_a = 35$ nm) for five different E_{laser} values (1.92 eV, 2.18 eV, 2.41 eV, 2.54 eV, and 2.71 eV). The spectra are normalized to the G-band intensity, and clearly the $(I_{\text{D}}/I_{\text{G}})$ ratio is strongly dependent on E_{laser}. Figure 13.11b shows the Raman spectra using $E_{\text{laser}} = 1.92$ eV for samples with different T_{htt} values, thereby giving rise to samples with different crystallite sizes L_{a} [404].

Figure 13.12a shows a plot of $(I_{\text{D}}/I_{\text{G}})$ vs. $1/L_{\text{a}}$ for all samples and using the five different E_{laser} values from Figure 13.11. Noting that $I_{\text{D}}/I_{\text{G}}$ for a given sample is strongly dependent on E_{laser}, we see that all these curves collapse on to the same curve in the $(I_{\text{D}}/I_{\text{G}})E_{\text{laser}}^4$ versus L_{a} plot shown in Figure 13.12b, demonstrating that the ratio $I_{\text{D}}/I_{\text{G}}$ is inversely proportional to the fourth power of E_{laser}. Thus, a general equation is obtained for the determination of the nanographite crystallite

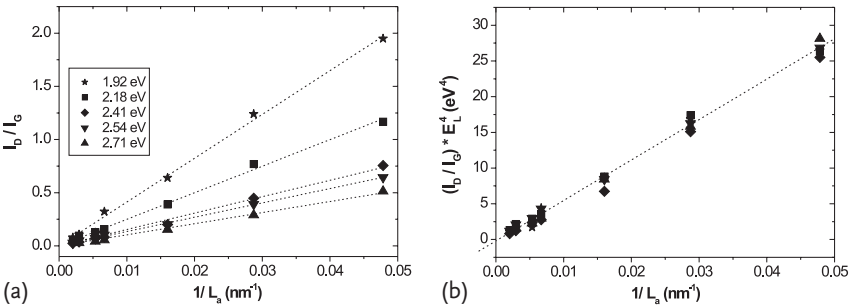

Figure 13.12 (a) The intensity ratio $I_{\text{D}}/I_{\text{G}}$ for nanographite samples is plotted versus $1/L_{\text{a}}$ using five different laser excitation energies. (b) All curves shown in part (a) collapse onto the same curve in the $(I_{\text{D}}/I_{\text{G}})E_L^4$ vs. $(1/L_{\text{a}})$ plot where $E_L \equiv E_{\text{laser}}$ [404].

size L_a using any laser line in the visible range [404]

$$L_a(nm) = \frac{560}{E_{laser}^4}\left(\frac{I_D}{I_G}\right)^{-1} = (2.4\times10^{-10})\lambda_{laser}^4\left(\frac{I_D}{I_G}\right)^{-1}, \quad (13.11)$$

where the laser excitation is given in terms of both E_{laser} (eV) or wavelength (nm).

13.3.4
Absolute Raman Cross-Section

Measuring the absolute cross-section for the Raman scattering processes is not trivial, since the Raman signal depends strongly on the specific setup (specific optics), on alignment, excitation wavelength. This is the reason why the intensity ratio I_D/I_G has been used systematically for quantifying disorder. Some argue that the intensity ratio $I_D/I_{G'}$ should be chosen because both the D-band and G′-band involve a very similar phonon (intervalley iTO, $q \approx 2k$). However, the D and G′-bands differ strongly in energy, and different Raman setups would give different responses.

However, Cançado *et al.* [405] have done all the calibration procedures for measuring the absolute Raman cross-section of the D, G, D′ and G′-bands (see Section 5.5). In this work, the dependence of I_D/I_G on L_a was shown to come from I_D, while I_G was found to be independent of L_a within the measured L_a range (from 20 to 500 nm). For the E_{laser} dependence, the double resonance features were shown to be E_{laser} independent, while the I_G shows the E_{laser}^4 dependence expected from scattering theory (see Section 5.5 and [405]). It is not yet known if the E_{laser}^4 dependence will be also observed for zero-dimensional (e. g., ion-induced) defects. Actually, one of the open fields in the Raman spectroscopy of sp^2 carbons is what rules determines intensity of the double resonance features. Sato *et al.* (see Section 13.1 and [395]) and Basko [370] have done some theoretical work on this topic, but the results are still not at the level of explaining experimental observations.

13.4
Defect-Induced Selection Rules: Dependence on Edge Atomic Structure

Besides defect quantification, it is important to discuss how disorder depends on the specific defect. An example of a result that was successful in distinguishing different defects from one another is the study of the edge of a graphite sample, analyzing the orientation of the carbon hexagons with respect to the edge axis, thereby distinguishing the so-called zigzag edge arrangements from the armchair or random atomic edge structures [161]. As discussed here, the armchair (zigzag) edge structure can be identified spectroscopically by the presence (absence) of the D-band. This effect can be understood by applying double resonance theory to a semi-infinite graphite crystal and by considering the one-dimensional character of the defect, as discussed below.

The most common case of disorder-induced features in the Raman spectra of graphite-related materials occurs in samples formed by aggregates of small crystallites. In this case, the crystallite boundaries form defects in real space. Since the crystallites have different sizes and their boundaries are randomly oriented, the defect wave vectors exhibit all possible directions and values. Therefore, the existence of a defect with momentum exactly opposite to the phonon momentum is always possible, giving rise to double resonance processes connecting any pair of points on the circles around the K and K' points. In this case, the intensity of the D-band is isotropic and does not depend on the light polarization direction. However, in the case of edges, the D-band intensity is anisotropic because the double resonance process cannot then occur for any arbitrary pair of points. Since, the edge defect in real space is well localized in the direction perpendicular to the edge, it is completely delocalized in this direction in reciprocal space and, therefore, the wave vector of such a defect assumes all possible values perpendicular to the step edge. Hence, the defect associated with a step edge has a one-dimensional character and it is only able to transfer momentum in the direction perpendicular to the edge.

Figure 13.13a shows the edges with zigzag (top) and armchair (bottom) atomic structure, separated from each other by 150°. The wave vectors of the defects associated with these edges are represented by $\boldsymbol{d}_a$ for the armchair edge and $\boldsymbol{d}_z$ for the zigzag edge. Figure 13.13b shows the first Brillouin zone of 2D graphite oriented according to the lattice in real space, as shown in Figure 13.13a. Note that for intervalley scattering, only the armchair $\boldsymbol{d}_a$ vector is able to connect points belonging to circles centered at two nonequivalent K and K' points. Considering usual laser energies (< 3 eV), the radius of the circles around the K' and K points are not large

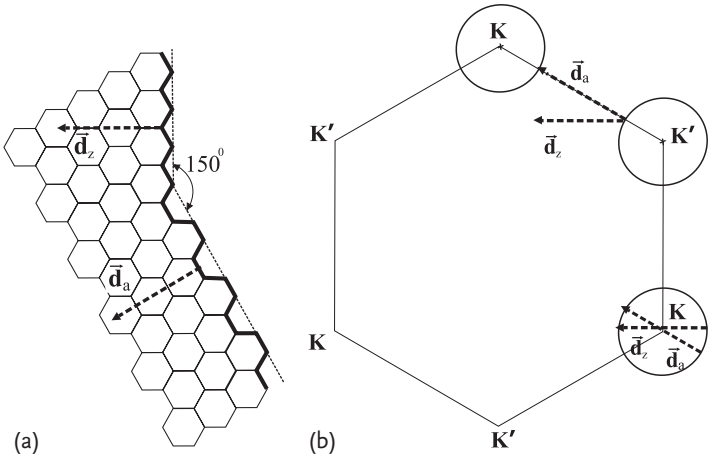

Figure 13.13 (a) Schematic illustration of the atomic structure of edges with the zigzag and armchair orientations. The boundaries can scatter electrons with momentum transfer along $\boldsymbol{d}_z$ for the zigzag edge, and $\boldsymbol{d}_a$ for the armchair edge. (b) First Brillouin zone of 2D graphite, showing defect-induced intervalley and intravalley scattering processes. Since $\boldsymbol{d}_z$ cannot connect the K and K' points, the defect-induced double resonance intervalley process is forbidden at zigzag edges [161].

enough to allow the connection of any $\boldsymbol{k}'$ and $\boldsymbol{k}$ states by a zigzag $\boldsymbol{d}_z$ vector. Therefore, the intervalley double resonance process associated with this defect cannot occur for a perfect zigzag edge. The mechanism depicted in Figure 13.13b thus shows that the D-band scattering process is forbidden in a zigzag edge [161].

On the other hand, the D′-band, around 1620 cm^{-1}, is given by an intravalley process, which connects points belonging to the same circle around the K (or K') point (see K point in Figure 13.13b). Therefore, the intravalley process can be satisfied by both $\boldsymbol{d}_a$ and $\boldsymbol{d}_z$ vectors and, for this reason, the observation of the D′-band should be independent of the edge structure.

Finally, when measuring an armchair edge, the D-band intensity will depend strongly on the light polarization direction with respect to the edge direction. The D-band intensity will be a maximum when the light is polarized along the edge, and zero when the light polarization is crossed with respect to the edge direction. This result is related to the theoretical calculations that predict an anisotropy in the optical absorption (emission) coefficient of 2D graphite (see Eq. (11.30) in Section 11.6.1), given by [220]:

$$W_{\mathrm{abs,ems}} \propto |\boldsymbol{P} \times \boldsymbol{k}|^2 \,, \tag{13.12}$$

where $\boldsymbol{P}$ is the polarization of the incident (scattered) light for the absorption (emission) process, and $\boldsymbol{k}$ is the wave vector of the electron measured from the K point. Correlating Eq. (13.12) with the D-band intensity dependence on the light polarization direction with respect to the edge is one of the problems at the end of this chapter.

In summary, the one-dimensional edge defect selects the direction of the electron and phonon wave vectors associated with the disorder-induced Raman process, and causes a dependence of the Raman D-band intensity on the atomic structure of the edge (strong for an armchair edge and weak for a zigzag edge). This discussion, therefore, represents an effort to improve our understanding of the influence of the defect structure on the Raman spectra of sp^2 carbon systems, which may be very useful to characterize defects in nanographite-based devices. The first experimental evidence for the selection rules discussed here was developed for a graphite boundary [161]. However, similar results have already been shown for monolayer graphene [407, 408]. Interestingly, up to now variations in the D-band intensity have been observed, but never a complete absence of the D-band together with the presence of the D′-band. This result indicates that, up to now, no perfect zigzag structure has been measured by Raman spectroscopy. It should be emphasized that Raman spectroscopy provides one easy method for distinguishing between armchair and zigzag edges. Of course, high resolution transmission electron microscopy provides another experimental method.

13.5
Specificities of Disorder in the Raman Spectra of Carbon Nanotubes

When moving to carbon nanotubes, the quantum confinement of the electronic structure will constrain the double resonance processes, similar to what has been discussed for the G′-band. A multi-peak structure [409] and an oscillatory dispersive behavior [410] can be observed for the D-band in SWNT bundles. For isolated tubes, unusually sharp features can be seen (a D-band with a FWHM down to $7\,\mathrm{cm}^{-1}$ [242]) due to quantum confinement effects. Furthermore, the D-band frequency also depends on the nanotube diameter, with the following result for 514 nm (2.46 eV) laser excitation:

$$\omega_{\mathrm{D}} = 1354.8 - 16.5/d_{\mathrm{t}}\,, \tag{13.13}$$

which is in rough agreement with the D-band being a one-phonon process related to the G′-band (see Eq. (12.11)).

Some efforts have been made to quantify disorder in SWNTs, by studying irradiated samples [411], and SWNTs cut to different lengths [412]. Clear enhancement of the D-band is observed with increasing defect density or with reducing nanotube lengths. However, because of the lack of direct real-space characterization, the results are not as quantitative as the results obtained in graphene [194] and in nanographite [404], as discussed in Section 13.3.

Some aspects are still unclear such as why the D-band in metallic SWNTs is usually more intense than in semiconducting tubes. Although some theoretical efforts based on the double resonance process have addressed this problem [413], the predictions are still incomplete. It is also important to mention that the double resonance process could give rise to a multi-peak structure in the G-band of SWNTs. It was then proposed that the several peaks in the G-band spectra of defective SWNTs could originate from the double resonance process [237, 414], as discussed below.

Figure 13.14 shows the G-band Raman spectra obtained from a SWNT fiber at two different locations, as shown in the inset of Figure 13.14a [415]. The upper spectrum comes from location **1**, at the center of the fiber. Figure 13.14b shows the G-band spectrum from location **2**, which is at the edge of the same fiber, where misalignment and defects (structural and impurities) are expected. The G-band intensity is much lower in location **2**, about 35 times less intense than in location **1**. Many peaks are observed in the spectrum at location **2**, clearly different from the spectrum at location **1**. Eight Lorentzian peaks were used for fitting the spectra at location **2**, which can be related to first-order allowed Raman peaks and to several different double resonance defect-induced peaks. For example, the inset to the lower panel of Figure 13.14 shows the E_{laser} dependence of the two peaks indicated by arrows. The solid curves in this inset are predictions for the E_{laser} dependence of the G-band double resonance features [160, 237]. The dispersive peak seems to agree well with a double resonance mechanism, while a nondispersive behavior fits the lower frequency peak observed in location **2**, which can be assigned as the first-order Raman-allowed TO G-band. It is not clear at this time how these peaks are related to specific edge defects and, again, more effort is needed for a quantitative

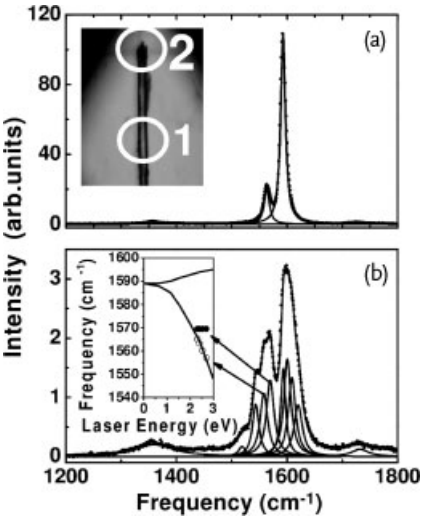

Figure 13.14 G-band resonance Raman spectrum from a fiber of aligned SWNT bundles ($E_{laser} = 2.71\,eV$). (a) The inset shows an optical image of the sample. The spectrum was taken from location **1** (see inset in (a)) with the light polarized along the fiber direction, and the spectrum in (b) was acquired from location **2**. The inset to (b) shows the E_{laser} dependence of the two peaks indicated by arrows. The solid curves in this inset are predictions for the E_{laser} dependence of the G-band double resonance features [415].

analysis of the disorder-induced features in carbon nanotubes, to make the RRS technique a more powerful tool for the characterization of disorder in sp^2 carbon materials.

13.6
Local Effects Revealed by Near-Field Measurements

Besides breaking momentum conservation, the presence of disorder is expected to change the local electron and phonon structure. The G′-band (see Chapter 12) is not a disorder-induced feature but it can nevertheless be used to probe changes in the electronic and vibrational structure related to disorder. The 2D vs. 3D stacking order of graphene layers is one example where the G′-band provides important information (see Section 12.2.4). Highly crystalline 3D graphite shows two G′ peaks (see Figure 12.8e). When the interlayer stacking order is lost, a one-peak feature starts to develop, identified with 2D graphite, and the peak is centered near the middle of the two peaks in the G′ lineshape from ordered graphite (see Figure 12.8f) [394]. More interesting, localized emission of a red-shifted G′-band was observed and is related to the local distortion of the nanotube lattice by a negatively charged defect. The defect position was initially located by local variations in the D-band intensity as described below [191].

Figure 13.15 shows near-field Raman and near-field photoluminescence spectra and their related spatial maps for an individual SWNT. The near-field technique can generate spectral information with spatial resolution Δx below the diffraction limit ($\Delta x \sim \lambda_{laser}/2$) [416]. In particular, Figure 13.15a,b show the photoluminescence and Raman spectra, respectively, with $\Delta x \sim 30\,nm$. The near-field microscopy measurements from the same SWNT are shown in Figure 13.15c–f. Figure 13.15c represents the near-field photoluminescence image of this SWNT, where the image contrast is provided by spectral integration over the photoluminescence peak centered at $\lambda_{em} = 900\,nm$ (see Figure 13.15a). The most striking feature in this image is the high degree of spatial localization of the photoluminescence emission along the SWNT. This is evident by inspection of the extended topography image of the nanotube shown in Figure 13.15f, and also of the near-field Raman image of

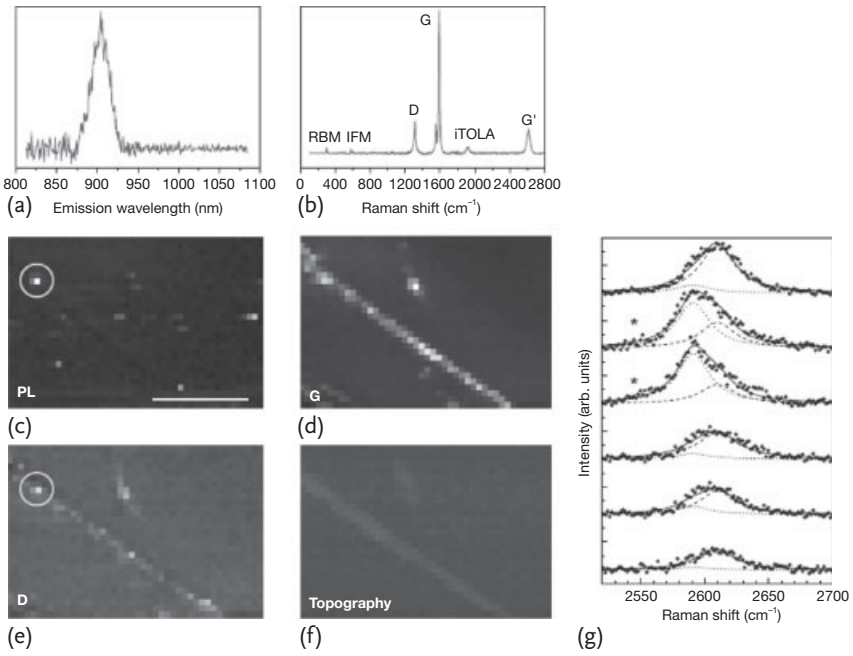

Figure 13.15 Localized excitonic emission in a semiconducting SWNT. (a) Photoluminescence emission at $\lambda_{em} = 900\,nm$. (b) Raman spectrum recorded from the same SWNT. The spectral position of the RBM, $\omega_{RBM} = 302\,cm^{-1}$, together with the $\lambda_{em} = 900\,nm$ information, leads to the (9,1) assignment for this tube. (c) Near-field photoluminescence image of the SWNT revealing localized excitonic emission. (d–e) Near-field Raman imaging of the same SWNT, where the image contrast is provided by spectral integration over the G and D-bands, respectively. (f) Corresponding topography image. The circles indicate localized photoluminescence (c) and defect-induced (D-band) Raman scattering (e). The scale bar in (c) denotes 250 nm. (g) Evolution of the G′-band spectra near the defective segment of the (9,1) SWNT. The spectra were taken in steps of 25 nm along the nanotube, showing the defect-induced G′ peak (dotted Lorentzian). The asterisks denote the spatial locations where localized photoluminescence and defect-induced D-band scattering were measured (see circles in (c) and (e), respectively) [191].

the G-band, with a peak intensity near 1590 cm^{-1} shown in Figure 13.15d. While from Figure 13.15d we observe that the G-band Raman scattering is present along the entire length of nanotube, from Figure 13.15e we observe an increased defect-induced (D-band, 1300 cm^{-1}) Raman scattering intensity localized in the *same* region where exciton emission was detected. Defects are known to act as trapping states for electron–hole recombination (i. e., exciton emission), thereby providing insights into the correlations observed between Figure 13.15c,e.

Interestingly, when measuring the Raman spectra across the defective spot, sudden changes in many Raman features are observed. Maciel *et al*. [191] have shown that substitutional doping in SWNTs causes changes in the G′-band spectra due to charge-induced renormalization of the electronic and vibrational energies. Figure 13.15g shows the G′-band measured on the same SWNT, moving along the position where the local D-band and photoluminescence emission is observed (circle in Figure 13.15e). The two spectra marked by "*" in Figure 13.15g were obtained at this defect location, and a new peak is observed at the G′-band. The frequency and intensity of this new peak depend on the type and level of doping, respectively [417–419]. This makes the G′-band a probe for studying and quantifying doping, which is more accurate than the D-band, since the D-band can also be related to amorphous carbon and any other defective sp^2 structure.

13.7 Summary

This chapter discusses how Raman spectroscopy can be used to probe defects in sp^2 nanocarbons. The break-down of momentum conservation together with the double resonance mechanisms make E_{laser}-dependent resonance Raman spectroscopy a powerful probe for electronic and phonon dispersion relations. Like the two-phonon double resonance peaks, the disorder-induced peaks represent a breakthrough in optical spectroscopy, because probing the phonon dispersion inside the Brillouin zone is usually done solely with neutron, electron or X-ray scattering, due to momentum conservation considerations. Besides, the possibility to probe particle size, layer stacking, defect concentration, edge structure and doping, and individual defects shows new power for optical spectroscopy techniques, that goes beyond the simple analysis of crystalline lattices. Here nanoscience is making possible the study of materials science from a completely new perspective.

The phenomenological model presented in Section 13.3.2 describes well the evolution of the D-band intensity with increasing defect density. However, the physics ruling the intensity of the double resonance features, in general, is an open question. It is clear that when moving into the use of near-field Raman spectroscopy, a new world opens for exploration. Although this research area still presents several technical difficulties, near-field techniques seem to provide major future opportunities for Raman spectroscopy studies of nanocarbons.

Problems

[13-1] In Eq. (13.3), if V is periodic in the crystal, show that the matrix elements vanish except for $k' = k$ in the first Brillouin zone. Here use the fact that $\langle\phi(R_{s'})|V|\phi(R_s)\rangle$ depends only on $R_{s'} - R_s$. Show that the matrix elements have a large value for $k' = k + G$, where G is a reciprocal lattice vector.

[13-2] Obtain the next order correction to the wavefunction of Eq. (13.5) by substituting $\Phi(k')$ iteratively for $\Psi^c(k')$ in the last term of Eq. (13.5).

[13-3] Using the previous results, obtain Eq. (13.6).

[13-4] Higher-order correction terms can be obtained similarly by substituting $\Phi(k')$ iteratively for $\Psi^c(k')$ in the last term of Eq. (13.5). Using this approach, get a general expression for $\Phi(k')$ and $M_{k'k}$.

[13-5] After consulting some textbook on scattering theory, explain that the T-matrix is expressed by $T = V + VG_0T$ or $T = V + VGV$, where $V \equiv H - H_0$ is an impurity potential operator and where H and H_0, respectively, denote the perturbed and nonperturbed Hamiltonians, while $G = (E - H)^{-1}$ and $G_0 = (E - H_0)^{-1}$ denote perturbed and nonperturbed Green's function. Using proper basis functions shows that we can make a matrix for each operator and get the T-matrix.

[13-6] In scattering theory, the S-matrix is also frequently used. Explain the difference between the T-matrix and the S-matrix. What are the advantages and disadvantages for using the T and S matrices?

[13-7] Considering the electron and phonon dispersions near the K point in graphene, derive a quantitative description which explains why $\omega_{G'} \neq 2\omega_D$ for one-phonon vs. two-phonon processes in the double resonance of the iTO phonon $\omega(q)$ branch near the K point, where q denotes the phonon wave vector.

[13-8] Sketch all the possible defect-induced double resonance one-phonon processes in monolayer graphene for Stokes and anti-Stokes, intravalley and intervalley processes.

[13-9] Consider the electronic dispersion of graphene in the linear approximation, that is, $E^{\pm}(k) = \pm\hbar v_F|k|$, where v_F is the Fermi velocity of the electrons given by $v_F = \sqrt{3}(\gamma_0 a/2\hbar)$, and $a = \sqrt{3}a_{C\text{–}C}$ is the lattice constant of graphene and $a_{C\text{–}C} = 1.42$ Å is the nearest neighbor carbon–carbon distance. Calculate the pair of (q, k) wave vectors which would fulfill the one-phonon defect-induced double resonance conditions for $E_{laser} = 1.98$ eV and 2.41 eV. Considering the phonon dispersion in Figure 13.5b, give the approximate frequency for all the defect-induced Raman peaks that should be observed for these two laser lines. Check your results against the values in Figure 13.5a.

[13-10] Calculate the number of Ar^+ ion-induced defects per C atom expected for a 10^{11} Ar^+/cm^2 and a 10^{15} Ar^+/cm^2 ion bombardment dose on a monolayer of graphene.

[13-11] In our phenomenological model for the D-band intensity dependence on Ar^+ ion impacts, consider S_S, S_A and S_T as the structurally damaged, activated and total areas of the graphene sheet, respectively, and N as the number of Ar^+ ion collisions. Derive Eq. (13.8) using rate equations (for dS_S/dN and dS_A/dN) and considering the initial conditions $f_S = 0$ and $f_A = 0$ for $\sigma = 0$.

[13-12] Derive Eq. (13.9). Suppose that the width δ of the boundary is responsible for the E_{laser}^4 dependence observed experimentally for I_D/I_G. How should δ vary with E_{laser} to obtain this relation? In this case, what would be the expected E_{laser} dependence of I_D/I_G for point defects inducing the D-band?

[13-13] Show that $(560/E_{laser}^4) = (2.4 \times 10^{-10}\lambda^4)$, as shown in Eq. (13.11).

[13-14] Explain why Eq. (13.12) is responsible for the polarization dependence observed for the D-band in armchair edges, and show that a $I_D \propto \cos\theta^4$ dependence is expected for the D-band intensity when both the incident and scattered light are analyzed along an angle θ with the edge direction.

[13-15] Calculate the intervalley matrix element $M_{k'k}$ for an armchair edged nanoribbon of width L_a. Here we assume that an electron is reflected at the armchair edge. Show that this assumption predicts a width dependence for the D/G intensity ratio given by $I_D/I_G \propto L_a^{-2}$. Such a relation has not been observed experimentally, showing that more work (both experimental and theoretical) is still needed.

[13-16] The G′-band was observed to shift to higher frequencies under acceptor (*p*-type) doping, and to lower frequencies under donor (*n*-type) doping. Explain qualitatively which doping-induced changes should happen to the electronic and/or phonon dispersion relations to generate such a shift.